Supporting information for
Structural snapshots of OxyR reveal the peroxidatic mechanism of H₂O₂ sensing

Brandán Pedre[a,b,c,*], David Young[a,b,c,*], Daniel Charlier[d], Álvaro Mourenza[e], Leonardo Astolfi Rosado[a,b,c], Laura Marcos-Pascual[e], Khadija Wahni[a,b,c], Edo Martens[a,c], Alfonso G. de la Rubia[e], Vsevolod V. Belousov[f,g,h], Luis M. Mateos[e,2], and Joris Messens[a,b,c,2]

a. VIB-VUB Center for Structural Biology, VIB, B-1050 Brussels, Belgium
b. Brussels Center for Redox Biology, Vrije Universiteit Brussel, B-1050 Brussels, Belgium
c. Structural Biology Brussels, Vrije Universiteit Brussel, B-1050 Brussels, Belgium
d. Research Group of Microbiology, Vrije Universiteit Brussel, B-1050 Brussels, Belgium
e. Department of Molecular Biology, Area of Microbiology, University of León, 24071 León, Spain
f. Shemyakin-Ovchinnikov Institute of Bioorganic Chemistry, 117997 Moscow, Russia
g. Pirogov Russian National Research Medical University, 117997Moscow, Russia
h. Institute for Cardiovascular Physiology, Georg August University Göttingen, 37073, Göttingen, Germany

[1]These authors contributed equally to this work

[2]To whom correspondence should be addressed: Joris Messens, Structural Biology Research Center, Redox Signaling lab, Vlaams Instituut voor Biotechnologie (VIB), Vrije Universiteit Brussel (VUB), Pleinlaan 2, 1050 Brussels, Belgium, Phone: +32 2 6291992, Fax: +32 2 6291963; E-mail: joris.messens@vib-vub.be
Luis M. Mateos. Department of Molecular Biology, Area of Microbiology, University of León, 24071 León, Spain; E-mail: luis.mateos@unileon.es

Methods

Intrinsic fluorescence changes upon oxidation
Experiments were performed in 100 mM sodium phosphate buffer pH 7.4 and 0.1 mM diethylene triamine pentaacetic acid (DTPA) at 25°C. The intrinsic fluorescence emission spectra (λ_{exc} = 295 nm) of (i) reduced WT RD-*Cg*-OxyR (1 µM), (ii) 100 µM H_2O_2-treated RD-*Cg*-OxyR for 1 min or (iii) 100 µM H_2O_2-treated RD-*Cg*-OxyR for 1 min followed by 20 min of 10 mM DTT incubation, were obtained using an LS55 luminescence spectrophotometer (PerkinElmer). Pre-steady-state kinetic measurements were performed using a stopped-flow apparatus (1.1 ms mixing time) coupled with a fluorescence detector (<320 nm cut-off filter) (Applied Photophysics SX20). 1 µM of reduced RD-*Cg*-OxyR variants was mixed with different concentrations of H_2O_2. For WT *Cg*-OxyR, experimental curves were fitted to single exponential curves (Y = A.e$^{(-kobs.t)}$ + offset), from which the observed rate constants (k_{obs}) were determined. The observed rate constants were plotted as a function of H_2O_2 concentration. The data was fitted to a hyperbolic equation k_{obs} = ([E_0]k_{cat}[H_2O_2])/(K_M + [H_2O_2]). For the T136V and H205A variants, the increasing curves were fitted to single exponential curves and the observed rate constants were plotted as a function of H_2O_2 concentration. The data were fitted to a linear equation.

Ferrous oxidation of xylenol orange (FOX) assay
FOX assay was used to determine the H_2O_2 consumption over time by the purified RD-*Cg*-OxyR variants and the *C. glutamicum* strains. 10 µL of the reaction mixture were mixed with 490 µL of the FOX reaction mix (100 µM xylenol orange, 250 µM ammonium ferrous sulfate, 100 mM sorbitol and 25 mM H_2SO_4), and incubated for 30 min at room temperature in darkness. At the end of the reaction, A_{560nm} was measured on a 96-well plate reader (SPECTRAmax 340PC, Molecular Devices). The H_2O_2 concentration was calculated based on a H_2O_2 standard curve. In the case of purified *Cg*-OxyR, 100 µM of the *Cg*-OxyR variants were mixed with 100 µM H_2O_2 in 100 mM sodium phosphate buffer, pH 7.4, at 25°C. 10 µL aliquots were taken after 10, 20, 30, 40, 50, 60, 90, 150 and 300 seconds. For the determination of the second-order rate constant in R278Q *Cg*-OxyR, 100 µM H_2O_2 was added to 100, 125, 150, 175 and 200 µM R278Q *Cg*-OxyR, and 10 µL aliquots were taken after 10, 20, 30, 40, 60, 90, 150, 300 and 600 seconds. In the case of the *C. glutamicum* strains (WT, Δ*oxyR*, Δ*oxyR* + WT*oxyR*, Δ*oxyR* + C206S*oxyR*, Δ*oxyR* + C215S*oxyR*), cells were grown on TSB at 30°C until reaching A_{600nm} = 1, then 8 mM or 40 mM H_2O_2 was added to the cell cultures. 10 µL aliquots were taken after 20, 40, 60, 80, 100, 120, 150, 200, 250 and 300 seconds.

Electrophoretic mobility shift assays (EMSA), DNase I footprinting and missing contact probing
Single 5'-end labeled DNA fragments were generated by PCR amplification with genomic DNA of *C. glutamicum* as template and as primers the oligonucleotides katA_EMSA_2 and katA_EMSA_1c (1) (Supplementary Table 1), one of which was 5'-end labeled with [γ^{32}P]-ATP and T4 polynucleotide kinase. Amplified fragments were purified by gel

electrophoresis on 6% polyacrylamide and recovered from gel. *Cg*-OxyR-DNA binding assays were performed at 25°C for 30 min in binding buffer (20 mM Tris/HCl, pH 7.5, 50 mM NaCl, 5 mM MgCl$_2$, 5 mM TCEP, 5% glycerol), in the presence of a large excess of non-specific competitor DNA (25 µg/ml sonicated salmon sperm DNA). Separation of free DNA from protein-DNA complexes was performed by migration on 6% polyacrylamide with Tris-borate-EDTA buffer (TBE; 89 mM Tris, 89 mM boric acid, 0.25 mM EDTA) as running buffer and at 8 V cm^{-1} for 3 hours. DNase I footprinting was performed as described previously, using 70, 120 and 400 nM WT/C206S/C215S *Cg*-OxyR under reducing and oxidizing conditions (2). Missing contact probing was performed as described previously, using 150, 225 and 300 nM reduced/oxidized *Cg*-OxyR (3). Reaction products were separated by electrophoresis on 8% polyacrylamide gels in denaturing conditions. Reference ladders and sparingly modified DNA for missing contact probing (3) were generated by treatment of the 5'-end labeled DNA fragments with citrate (purines) or hydrazine (pyrimidines) as described (4).

DNA polarimetry analyses
10 nM of 6-carboxyfluorescein (6-FAM)-labeled *katA* binding region (Sigma) were mixed with increasing concentrations of reduced or H$_2$O$_2$-treated WT or C206S *Cg*-OxyR at 25°C in polarimetry buffer (50 mM HEPES-NaOH, pH 7.5, 200 mM NaCl and 2 mM TCEP, or without TCEP under H$_2$O$_2$-treated conditions). Polarimetry measurements were performed on the SX20 stopped flow apparatus equipped with a fluorescence polarization accessory and 515 nm cut-off filters (λ_{ex} = 494 nm). Data was recorded when the reaction reached the equilibrium (minimum 5000 points), and at least 3 technical and 3 experimental replicates were performed for every condition.

Construction of Cg-*OxyR derivative strains in* C. glutamicum
For gene disruption of the *Cg-oxyR* gene, an internal fragment of the *oxyR* gene was PCR-amplified using the primer pair OxyR_dis_fw/rev (Supplementary Table 1). The amplified fragment was *Eco*RI/*Hind*III digested and cloned into the equivalently digested pK18mob plasmid(5). The obtained plasmid was used to transform the *E. coli* strain S17-1 (donor strain), and transformants used for integrative plasmid mobilization to the recipient strain *C. glutamicum* RES167 via conjugation and selection with kanamycin (12.5 µg/mL). PCR-amplification analysis and further fragment sequencing validated the correct chromosomal plasmid integration.
For *Cg*-OxyR complementation, the recombinant pET28a-derived plasmids pET_FLOxyR, pET_FLOxyR_C206S and pET_FLOxyR_C215S (Supplementary Methods) were firstly mutagenized to remove an internal *Bgl*II restriction site using the mismatched primer-pair OxyR_no*Bgl*II_fw/OxyR_no*Bgl*II_rev (Supplementary Table 1). The mutations are silent at the protein level. The clones lacking the *Bgl*II restriction site were selected by *Bgl*II digestion (target absent) of the isolated plasmids and further corroborated by gene sequencing. The selected plasmids were PCR-amplified using the primer-pair FLOxyR_fw/FLOxyR_rev (Supplementary Table 1), digested with *Nde*I/*Xho*I and the isolated fragments used to be subcloned with the equally digested pXHisNpro plasmid(6). The obtained recombinant plasmids were *Bgl*II digested and the individual 2 kbp cassettes [containing the *Cg-oxyR* gene variants under the control of the constitutive kanamycin promoter (P_{kan}-*oxyR*)] were further ligated to the bifunctional mobilizable vector pECM2 (*Bam*HI digested)(6), obtaining the recombinant plasmids pECOxyR-WT,

pECOxyR_C206S and pECOxyR_C215S. These plasmids were adequately transferred by conjugation to the ΔoxyR C. glutamicum strain.

In vivo H_2O_2-resistance assays

C. glutamicum strains were precultured overnight in trypticase soy broth (TSB) containing the adequate selective agent, and diluted 100-fold in fresh TSB media and grown until reaching A_{600nm} = 1. Then, cultures were washed and resuspended in an equal volume of water. Samples of 10 μL were disposed on dishes containing TSB agar (TSA) supplemented with different concentrations of H_2O_2 (0, 2, 4, 6, 8, 10, 12, 14, 16 mM) and further incubated to 30°C for 24-36 h.

RNA isolation from C. glutamicum

C. glutamicum strains were precultured overnight in lysogeny broth (LB) containing the adequate selective agent. The precultures were 100-fold diluted in 100 mL of LB and grown until reaching A_{600nm} = 1. For each strain, three conditions were applied: (i) a no H_2O_2 control; (ii) a 10 mM H_2O_2 dose for 10 min; (iii) a 10 mM H_2O_2 dose for 30 min. Cells were then harvested (5 min at 10,000 x g) and mixed with 1 mL of TRI Reagent® (Sigma-Aldrich). This suspension was transferred to a 2-mL Eppendorf tube containing 500 μL of diethylpyrocarbonate (DEPC)-treated 0.1 mm zirconia silica beds (Sigma-Aldrich). Cells were then lysed using a Fast-Prep FP120 cell disrupter (MPbiomedical, USA) with 4 x 45 s pulses at a speed setting of 6.0; then the tubes were stored at -80°C overnight. The RNA was then isolated following the protocol described elsewhere(7). This method is a combination of Trizol-based extraction (Tri Reagent®, Sigma-Aldrich) and purification using silica columns (Qiagen RNeasy kit, Qiagen GmbH). To avoid DNA contamination, samples were DNase treated twice, first using Turbo DNase (Ambion) and then again with the DNase provided Qiagen RNeasy kit. Purity and concentration of the isolated RNA samples were obtained by determining the $A_{260nm/280nm}$ with a NanoDrop 2000 (Thermo Fisher Scientific).

Real-Time Quantitative Reverse Transcription PCR of catalase transcription

1 μg of the isolated RNA was used as template to generate cDNA using the RETROscript™ reverse transcription kit (Ambion). Reaction mixture was achieved with: 1/20 of each cDNA product (or any negative control DNA sample), 200 nM specific primer pairs (Suppelementary Table 1), 1X KAPA SYBR® FAST qPCR Kit Master Mix (2X) (KAPA Biosystems) and H_2O until reaching 20 μL. Primer-pairs for the target genes were developed making use of the "Primer Express Software v2.0" program from Applied Biosystems, with sequences shown on Supplementary Table 1. Amplified PCR products were 50-100 nucleotides long. 16S rDNA was used as non-inducible control. The obtained results were processed using StepOne™ Software v2.0 and cycle threshold (C_t) was obtained. Three experimental replicates were performed, with each being the average of three technical replicates.

Construction of the plasmids for Cg-*OxyR recombinant expression*

Full-length (FL) and regulatory domain (RD) of *C. glutamicum* OxyR were amplified with the primer pairs FLOxyR_fw/FLOxyR_rev and RDOxyR_fw/RDOxyR_rev, respectively (Supplementary Table 1). PCR-amplified fragments were *Nde*I/*Xho*I digested and ligated

with equivalently digested expression vector pET28a, obtaining plasmids pET_FLOxyR and pET_RDOxyR.

Site-directed mutagenesis of Cg-*OxyR*

Mutations T107V, T136V, H205A, C206S, C215S and R278Q were introduced into the pET_FLOxyR or pET_RDOxyR plasmid by site-directed mutagenesis, using the QuikChange® Site-Directed Mutagenesis Kit (Stratagene, La Jolla, CA). Reaction mixtures contained 50 ng of template plasmid DNA and 125 ng of each primer (Supplementary Table 1). The triplets coding for the mutations are underlined in Supplementary Table 1. Mutations were confirmed by DNA sequencing.

Protein expression and purification

The recombinant expression vector pET28a_FLOxyR was introduced into *E. coli* C41(DE3); transformant colonies were isolated and grown at 37°C till A_{600nm} = 0.6 and then induced with 1 mM isopropyl-β-D-thiogalactopyranoside (IPTG) for 3.5 h at 37°C. The harvested cells were resuspended in 5 mM imidazole, 50 mM (4-(2-hydroxyethyl)-1-piperazineethanesulfonic acid (HEPES)-NaOH, pH 8.0, 1 M NaCl, 1 μg/ml Leupeptin, 0.1 mg/ml 4-(2-aminoethyl) benzenesulfonyl fluoride hydrochloride, 100 μg/ml DNaseI, 20 mM $MgCl_2$, and lysed using French press (20 kPsi, Constant Systems). The lysate was centrifuged at 18000 rpm at 4°C for 45 min, and the clarified supernatant was added to Ni^{2+}-Sepharose (GE Healthcare) affinity beads equilibrated in 50 mM HEPES-NaOH, pH 8.0, 1 M NaCl, 5 mM imidazole buffer. The mixture was incubated for 30 min at 4°C and packed on a column. After a wash step with 50 mM HEPES-NaOH, pH 8, 1 M NaCl, 5 mM imidazole buffer, and eluted with a linear gradient to 500 mM imidazole in the same buffer. The protein was further purified on a Superdex75 PG (16/90) column (GE Healthcare) equilibrated in 20 mM Tris/HCl pH 8.0, 500 mM NaCl, 1 mM EDTA and 0.5 mM DTT. To cleave the His-tag, bovine thrombin (Calbiochem) was added at 0.2 U/mg, and incubated overnight at 4°C. A second size-exclusion chromatography with Superdex75 PG (16/90), equilibrated in 20 mM Tris/HCl pH 8.0, 500 mM NaCl and 2 mM TCEP, was used to remove the His-tag and thrombin. His-tag cleavage was verified on non-reducing SDS-PAGE. To prepare oxidized *Cg*-OxyR, unless stated otherwise, WT *Cg*-OxyR was treated with a 5-fold molar excess of H_2O_2, incubated at 25°C for 3 min, and quickly desalted using a HiTrap desalting column (GE Healthcare), equilibrated in 20 mM Tris/HCl, pH 8.0 and 500 mM NaCl. For polarimetry experiments, the polarimetry buffer is used instead (see below).

For the RD-*Cg*-OxyR and the single residue mutants, expression followed similar conditions, except that the expression was at 30°C overnight. The Ni^{2+}-affinity chromatography followed the same conditions as in FL-*Cg*-OxyR. Following this step, bovine thrombin was added at 0.8 U/mg protein with simultaneous dialysis against 20 mM Tris/HCl pH 8.0, 300 mM NaCl and 1 mM DTT at 4°C overnight. Uncleaved RD-*Cg*-OxyR was removed via a second Ni^{2+}-affinity purification, and the cleaved protein was further purified on a Superdex75 PG (16/60) column (GE Healthcare) equilibrated in 20 mM Tris/HCl pH 8.0, 200 mM NaCl and 2 mM TCEP.

Peroxide and protein quantification

The concentration of H_2O_2 stock solutions (Sigma-Aldrich) was measured at 240 nm (ε_{240nm} = 43.6 $M^{-1}cm^{-1}$)(8). *Cg*-OxyR protein concentration was calculated with Bradford

reagent (Bio-Rad), using bovine serum albumin as calibration standard. The calculated protein concentrations refer to those of monomers.

Determination of OxyR oligomeric state in solution.

Different amounts of reduced/oxidized FL-Cg-OxyR (0.05, 0.15, 0.4 and 0.8 mg) were injected on a Superdex200 10/300 HR column (GE Healthcare), equilibrated in 20 mM Tris/HCl, pH 8.0 and 500 mM NaCl. To estimate the molecular weight, 250 µL of gel filtration standard (Bio-Rad) was injected. Elution peaks were determined by monitoring A_{280nm} on an ÄKTA pure fast-liquid protein chromatography device (GE Healthcare).

Generation of dsDNA of katA *promoter binding region*

Oligonucleotides of the *katA*_binding-region_fw and katA_binding-region_rev (Supplementary Table 1) were resuspended in annealing buffer (10 mM Tris/HCl, pH 7.5, 50 mM NaCl and 1 mM EDTA) and mixed equimolarly. Annealing was performed at 95°C for 3 min, with a slow cool down after the heating step. Oligonucleotides that did not anneal and other possible contaminants were removed via size-exclusion chromatography on a Superdex200 10/300 HR column (GE Healthcare).

Isothermal titration calorimetry experiments

ITC experiments were carried out using an iTC200 Microcalorimeter (Malvern). The syringe was filled with unlabeled ds *katA* binding region (Supplementary Table 1, 112 µM for reduced sample and 127 µM for oxidized sample) and the sample cell with *C. glutamicum* OxyR (42 µM for reduced sample and 37 µM for oxidized sample). All ITC measurements were carried out in 50 mM HEPES-NaOH, pH 7.5, 200 mM NaCl and 2 mM TCEP, or without TCEP under H_2O_2-treated conditions, at 12°C. The binding reaction started with one injection of 0.5 µL of *katA* binding region to prevent artifacts, followed by 25 injections of 1.56 µL at intervals of 180 s, reaching a final volume of 39.5 µL with a stirring speed of 500 rpm. The reference cell (200 µL) was loaded with water during all experiments and control titrations were performed to subtract the heats of dilution and mixing for each experiment. The data were analyzed with CHASM (9, 10) employing a nonlinear least squares fitting algorithm.

Supplementary Table 1: List of primers

Primer name	Sequence (5'>3')
FLOxyR_fw (*Dra*I[a], *Nde*I[b])	TAA<u>TTTAAA</u>[a]<u>CATATG</u>[b]AGCAATAAAGAGTACCGGCCCACACTC
FLOxyR_rev (*Dra*I[a], *Xho*I[b])	TAA<u>TTTAAA</u>[a]<u>CTCGAG</u>[b]TTACTGCGCTACCGCG
RDOxyR_fw (*Nde*I)	TAT<u>CATATG</u>GGTTCGCTCACTGGACCG
RDOxyR_rev (*Xho*I)	TATT<u>CTCGAG</u>TTACTGCGCTACCGCGAC
OxyR_T107Vfw	GTAGGCATCATCCCC<u>GTG</u>GCGGCTCCTTACATTTTG
OxyR_T107Vrev	CAAAATGTAAGGAGCCGC<u>CAC</u>GGGGATGATGCCTAC
OxyR_T136Vfw	CACATCGTCGAGGACCAA<u>GTC</u>AAGCATCTTCTCGCGTTG
OxyR_T136Vrev	CAACGCGAGAAGATGCTT<u>GAC</u>TTGGTCCTCGACGATGTG
OxyR_H205Afw	CTTCTCGACGACGGA<u>GCC</u>TGCCTCCACGAC
OxyR_H205Arev	GTCGTGGAGGCA<u>GGC</u>TCCGTCGTCGAGAAG
OxyR_C206Sfw	CTCGACGACGGACAC<u>AGC</u>CTCCACGACC
OxyR_C206Srev	GGTCGTGGAG<u>GCT</u>GTGTCCGTCGTCGAG
OxyR_C215Sfw	CAAATTGTGGACCTG<u>AGC</u>CGCCGCGGAGAC
OxyR_C215Srev	GTCTCCGCGGCG<u>GCT</u>CAGGTCCACAATTTG

OxyR_R278Qfw	CTGATGTCACCG<u>CAA</u>ACCAGCGCATTGGATTGGTG
OxyR_R278Qrev	CACCAATCCAATGCGCTGGT<u>TTG</u>CGGTGACATCAG
katA_EMSA_2(1)	TGCTGGCAGTTTACGTAAGG
katA_EMSA_1c(1)	TGCTGCTGACTTCTCAGACA
katA_bindingregion_fw	TGTAGACTATCAATCAGACTTAATCCATAGGTAACCCTCATAA AAGGAA
katA_bindingregion_rev	TTCCTTTTATGAGGGTTACCTATGGATTAAGTCTGATTGATAG TCTACA*
OxyR_dis_fw (*Eco*RI)	TAA<u>GAATTC</u>CGGCTCCTTACATTTTGC
OxyR_dis_fw (*Hind*III)	TAA<u>AAGCTT</u>AAGTCTTCGTCGTAGAGG
OxyR_no*Bgl*II_fw	GGATGAATATCCAGA<u>C</u>CTGGAACCTCACATCGTCG
OxyR_no*Bgl*II_rev	CGACGATGTGAGGTTCCAGGTCT<u>G</u>GATATTCTTCATCC
16S_rDNA_q_fw	CCAGCAGCCGCGGTAA
16S_rDNA_q_rev	ACGCCCAGTAATTCCGGAC
katA_q_fw	GCAACCGAGCCACGCGTC
katA_q_rev	CTCCTTGACGCGAGCGCC
oxyR_q_fw	TCATTTTGCAGCGCGCTTTC
oxyR_q_rev	CGCGACATTTTGCTTCAAGG

* 5' modified with 6-FAM in polarimetry assays

Supplementary Table 2: *katA* mRNA levels in several oxyR strains before and after 10 mM H_2O_2 treatment (n=3)

Strain	ΔC_t t=0	ΔC_t t=10min	ΔC_t t=30min
WT	17.85 ± 1.26	14.36 ± 0.66	16.31 ± 1.05
Δ*oxyR*	12.18 ± 0.74	10.84 ± 0.82	11.06 ± 0.83
Δ*oxyR* + WT*oxyR*	18.02 ± 2.48	16.41 ± 0.05	17.57 ± 0.04
Δ*oxyR* + C206S*oxyR*	14.99 ± 1.28	13.33 ± 1.67	13.38 ± 1.72
Δ*oxyR* + C215S*oxyR*	16.24 ± 0.92	14.33 ± 0.5	14.42 ± 0.28

Supplementary Table 3: *oxyR* mRNA levels in WT and Δ*oxyR* + WT*oxyR* under resting conditions (n=3)

| Strain	ΔC_t	*oxyR* fold-expression
WT	14.28 ± 3.03	1
Δ*oxyR* + WT*oxyR*	9.93 ± 0.56	20.34

Supplementary Figures
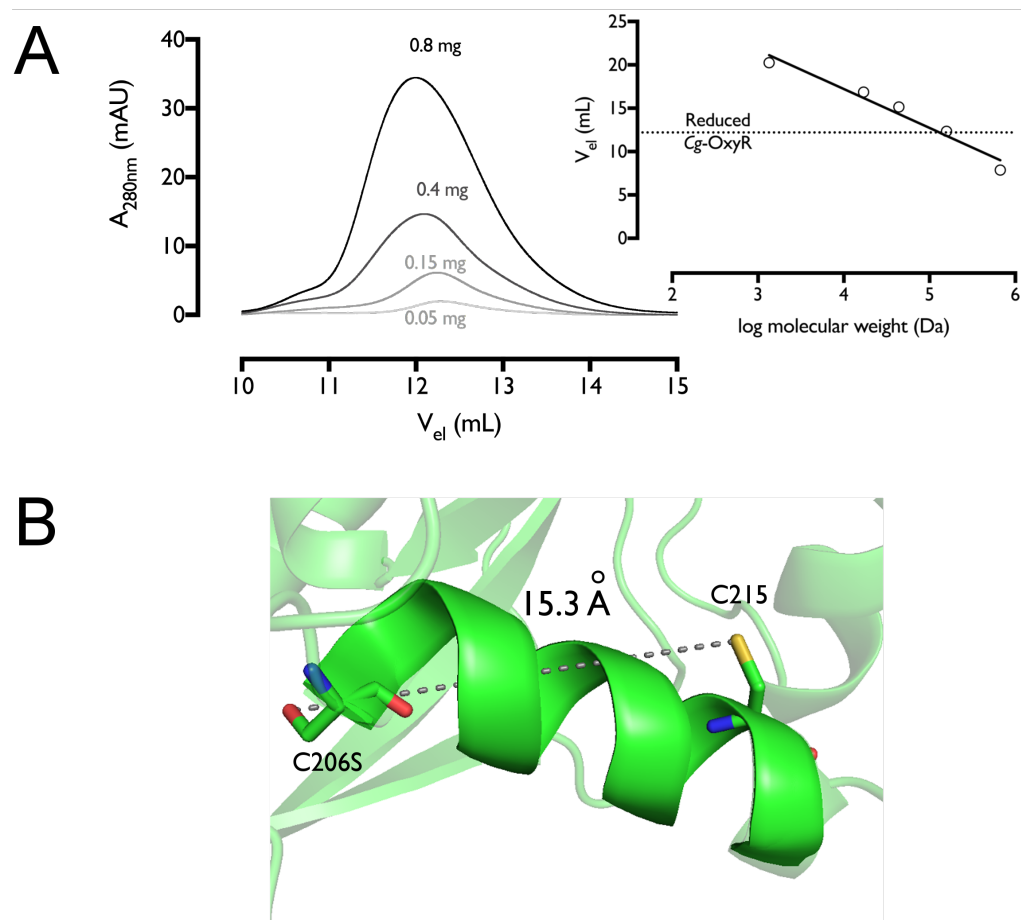
Supplementary figure 1: Structural details of C206S *Cg*-OxyR. (*A*) Size-exclusion chromatography shows that reduced *Cg*-OxyR is a tetramer in solution. Several amounts of *Cg*-OxyR were injected on a high-resolution Superdex200 column and protein elution was monitored (A_{280nm}). Inset shows the elution volumes of proteins used for calibration of the standard curve, and the position of reduced *Cg*-OxyR in the curve. (*B*) Close-up of the RDα3-helix where the two conserved cysteines are located (Cys206 was substituted by a serine). The distance between the residue side chains is highlighted.
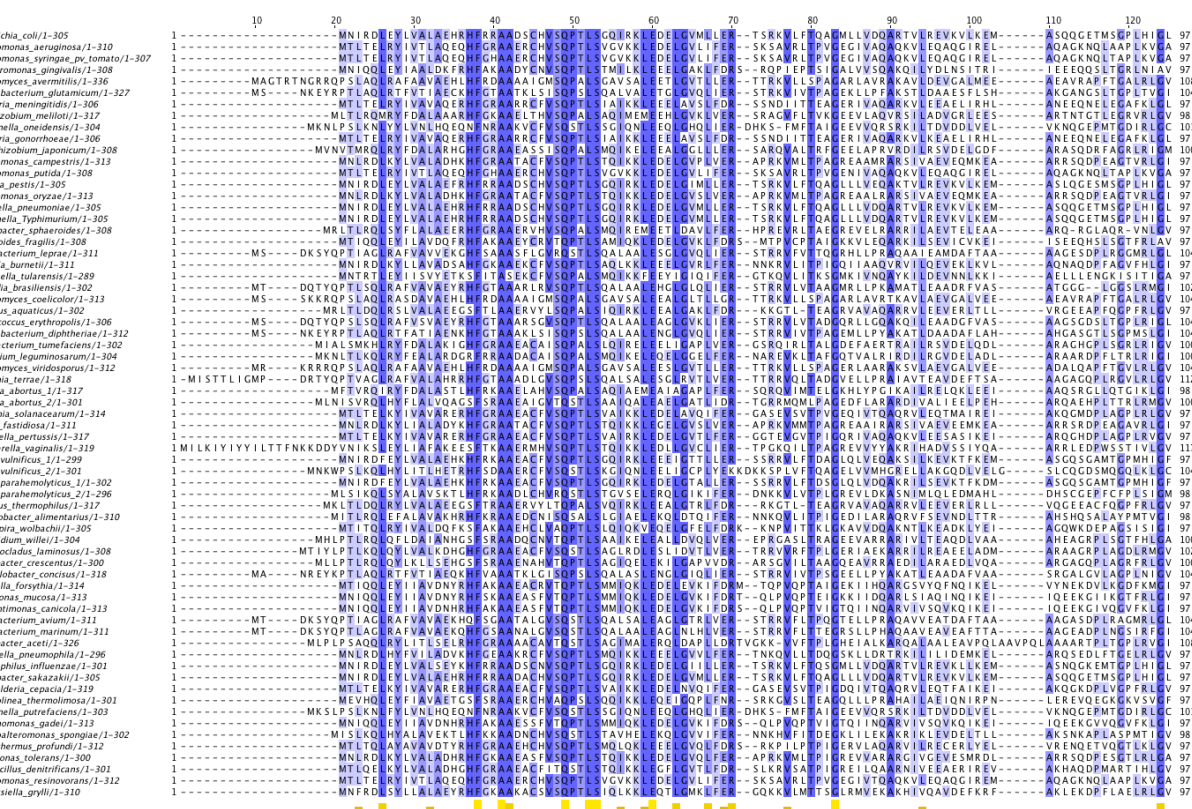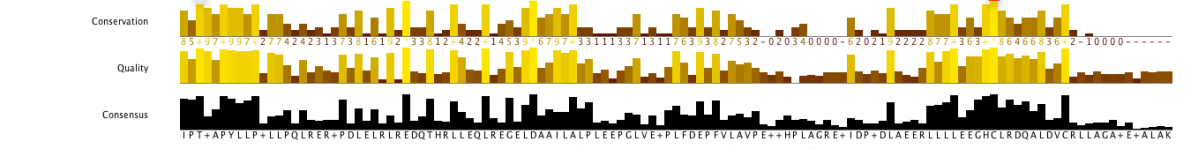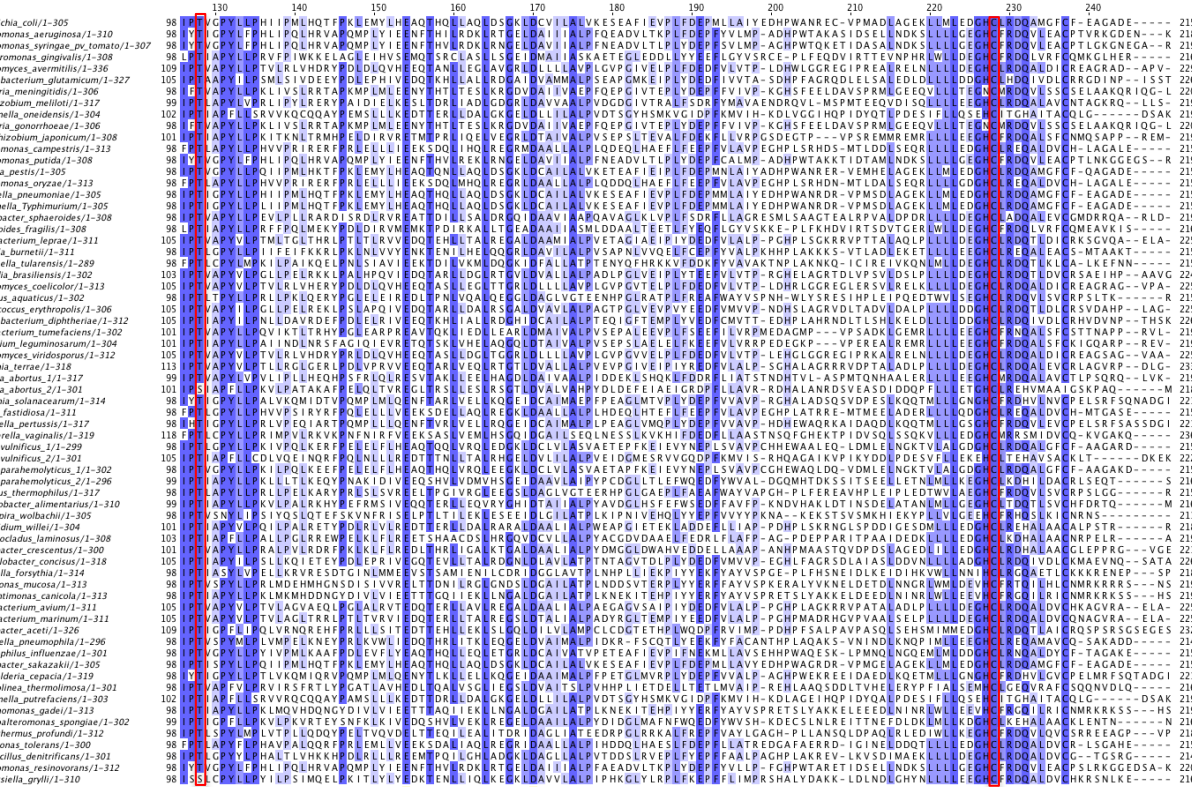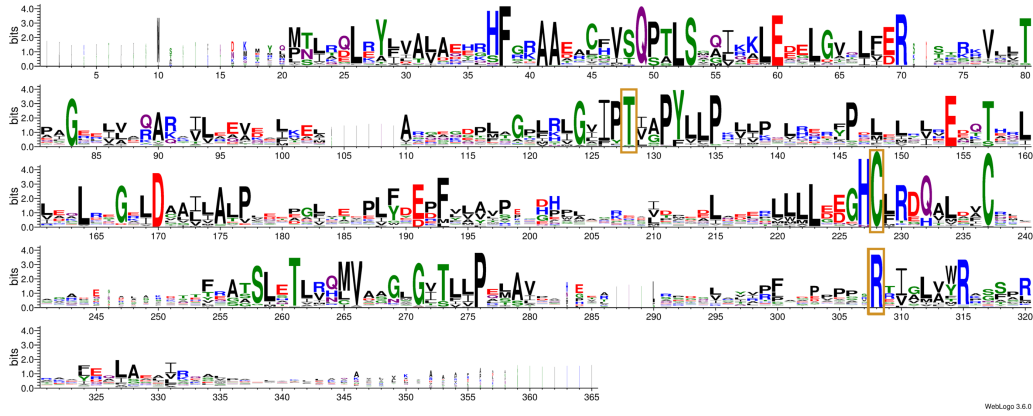
Supplementary figure 2: Sequence conservation provides evidence for a putative T/C/R triad in OxyR. (*A*) Multiple sequence alignment of 67 OxyR sequences. The sequences were taken from Uniprot or Uniparc database (http://www.uniprot.org), with some sequences taken from Genbank (highlighted next to the accession number): *E. coli*, P0ACQ4; *Pseudomonas aeruginosa*, Q9HTL4; *Porphyromonas gingivalis,* Q7MXD3; *Vibrio parahemolyticus* OxyR1, Q87L60; *Vibrio parahemolyticus* OxyR2, Q87IZ9; *Streptomyces avermitilis*, Q82IC7; *Neisseria meningitidis*, A1KRK4; *Shewanella oneidensis*, Q8EHA1; *Neisseria gonorrhoeae*, B4RR00; *Bradyrhizobium japonicum*, A0A023XTM7; *Corynebacterium glutamicum*, Q8NP91; *Yersinia pestis*, Q7CL10; *Xanthomonas oryzae*, Q5GWM0; *Salmonella enterica* bv. Typhimurium, Q7CPB9; *Rhodobacter spheroides*,

Q3J2P7; *Mycobacterium leprae*, P52678; *Coxiella burnetii*, Q83BM7; *Francisella tularensis*, Q5NHB0; *Streptomyces coelicolor*, Q9RN71; *Corynebacterium diphtheriae*, H2GUE0; *Agrobacterium tumefaciens*, A9CGX9; *Gordonia terrae*, H5UA91; *Brucella abortus* OxyR1, F8WJR3; *Brucella abortus* OxyR2, A0A0F6AUI6; *Ralstonia solanacearum*, F6FYN0; *Xylella fastidiosa*, Q87DD8; *Bordetella pertussis*, A0A0N2IP59; *Flavobacterium aquidurense*, A0A0Q0XTK2; *Thermus thermophilus*, Q5SM20; *Psychrobacter alimentarius*, A0A144Q2V7; *Leptospira wolbachii*, R8ZZY6; *Gardnerella vaginalis*, A0A1H1L1G5; *Anaerolinea thermolimosa*, GAP06981.1 (genbank); *Phormidium willei*, A0A168SMG3; *Mastigocladus laminosus*, WP_072046693 (genbank); *Caulobacter crescentus*, Q9A269; *Campylobacter concisus*, A0A1E7PIB2; *Tannerella forsythia*, G8UJV8; *Vibrio vulnificus* OxyR2, A0A087I947; *Vibrio vulnificus* OxyR1, A0A1V8MGK0; *Fermentimonas caenicola*, UPI00068192A4; *Mycobacterium avium*, X8A7G0; *Mycobacterium marinum*, O87324; *Acetobacter aceti*, B6EWX0; *Legionella pneumophila*, Q5ZUI3; *Burkholderia cepacia*, A0A0U4C6T6; *Haemophilus influenzae*, P44418; *Cronobacter sakazakii*, K8CVK8; *Rhizobium leguminosarum* bv. *viciae*, Q1M499; *Streptomyces viridosporus*, Q9X5P2; *Nocardia brasiliensis*, K0F8R7; *Thermus aquaticus*, A0A0M9AEN6; *Pseudomonas syringae* pv. tomato, Q88BF1; *Pseudomonas putida*, I3UV78; *Sinorhizobium meliloti*, F7X974; *Xanthomonas campestris*, Q8PCA2; *Bacteroides fragilis*, Q9FDN4; *Klebsiella pneumoniae*, R4Y427; *Rhodococcus erythropolis*, A0A0E4AD37; *Dysgonomonas gadei*, F5IXX1; *Pseudoalteromonas spongiae*, U1L317; *Rhodothermus profundi*, A0A1M6R944; *Luteimonas tolerans*, A0A1N6TRR4; *Thiobacillus denitrificans*, A0A106BR27; *Petrimonas mucosa*, A0A1G4G520; *Shewanella putrefaciens*, E6XNR3; *Pseudomonas resinovorans*, S6B241; *Rickettsiella grylli*, A8PL83. Multiple sequence alignment was performed with ClustalW; included in the MEGA software package(11). Color intensity represents sequence identity, and the conserved residues that belong to the OxyR T/C/R triad are highlighted in red. Figure was created using Jalview(12). (*B*) Weblogo (http://weblogo.threeplusone.com/create.cgi) obtained from the multiple sequence alignment of 67 OxyR sequences. Conserved residues of the active site T/C/R triad are highlighted in ocre.
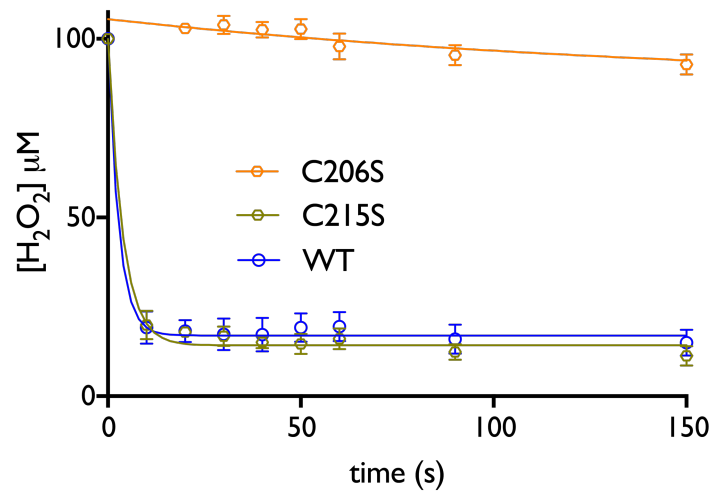
Supplementary figure 3: Only the first conserved cysteine (C206) is required for peroxidatic activity. WT, C206S and C215S *Cg*-OxyR were mixed with an equimolar amount of H_2O_2, and the H_2O_2 concentration was monitored in function of time with the FOX assay reagent. The lines correspond to single exponential fittings of the H_2O_2 consumption (n = 3). The error bars correspond to standard deviation (SD).
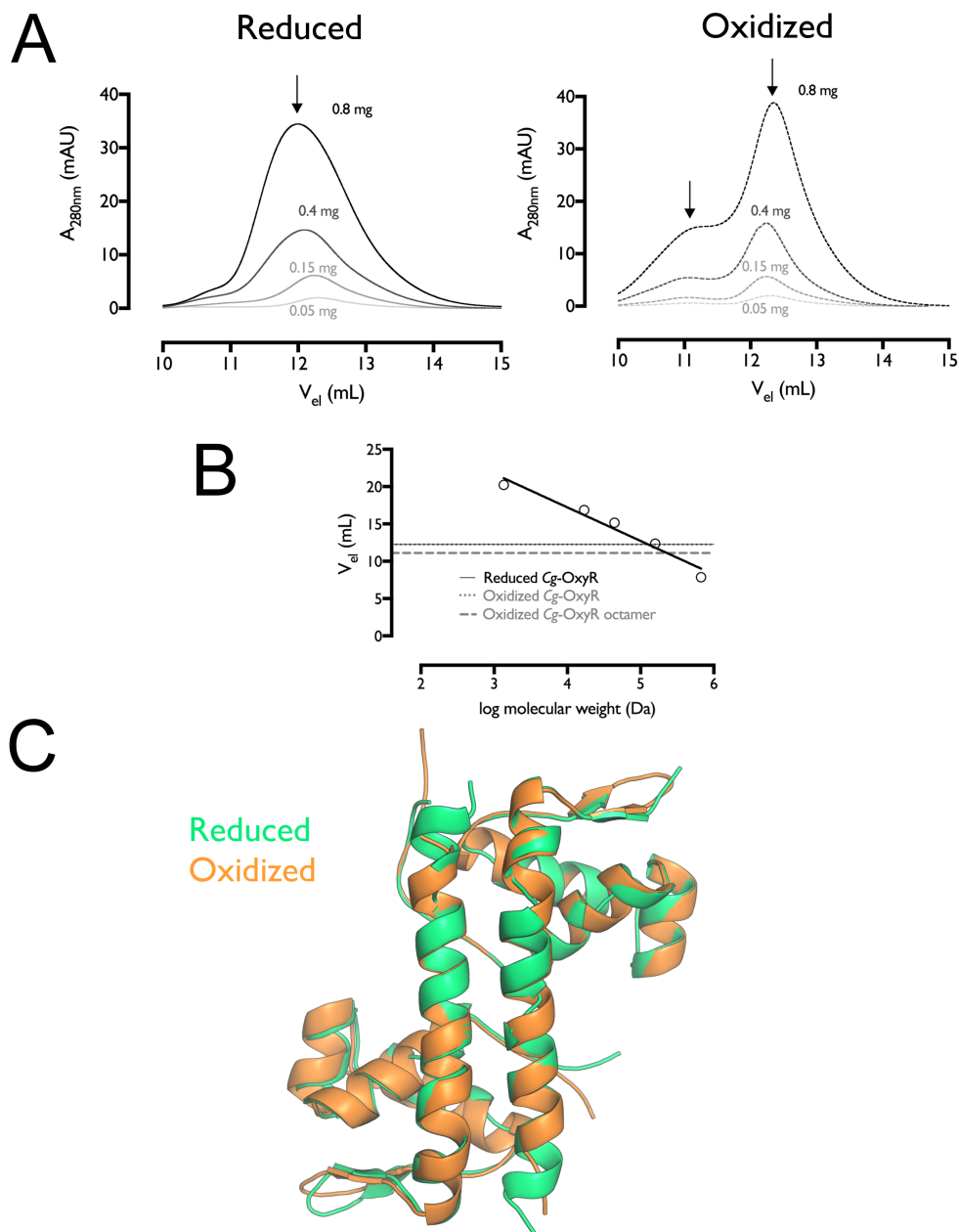
Supplementary figure 4: Oxidized *Cg*-OxyR is a tetramer in solution and shows no changes in the DBD. (*A*) Size-exclusion chromatography shows that oxidized *Cg*-OxyR (right) is mainly a tetramer in solution. Several amounts of oxidized *Cg*-OxyR were injected on a high-resolution chromatography column and protein elution was monitored at 280 nm. The elution profile of reduced *Cg*-OxyR is included on the left for comparison. The arrows indicate the elution peaks, corresponding to tetramers (for reduced and oxidized *Cg*-OxyR) and octamers (for oxidized *Cg*-OxyR). (*B*) Elution volumes of proteins used for calibration of the standard curve, and the position of injected 0.15 mg of reduced, oxidized and octamer oxidized *Cg*-OxyR in the curve. (*C*) Structure alignment of the DBD homodimers of reduced and oxidized *Cg*-OxyR.
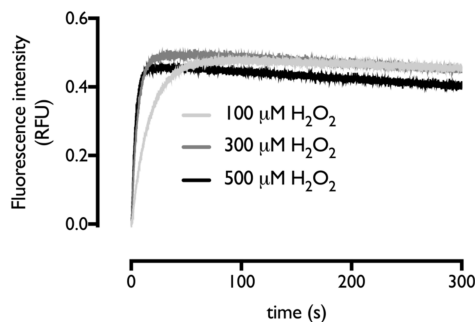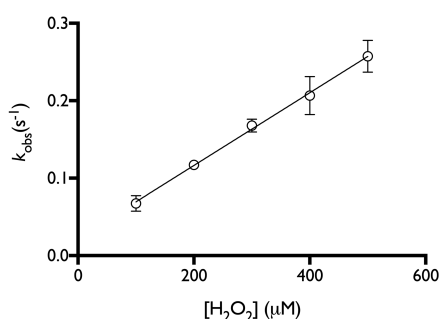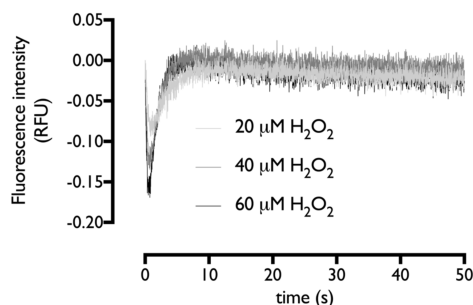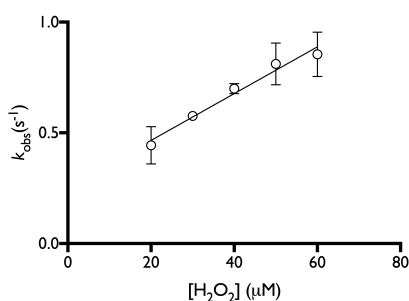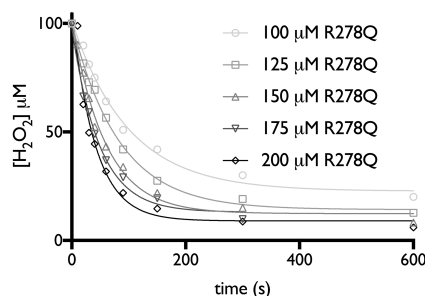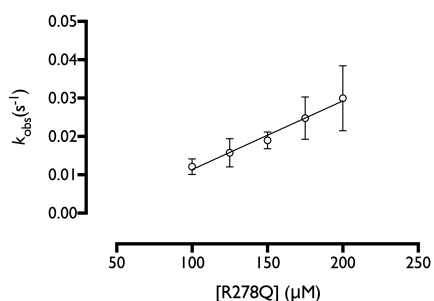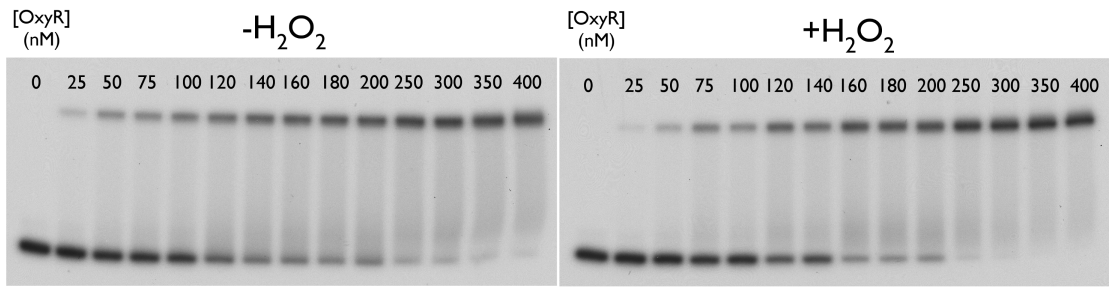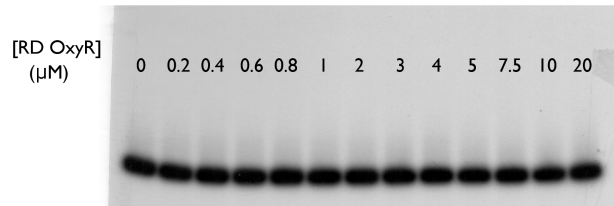
Supplementary Figure 5: *Cg*-OxyR shows rapid conformational changes upon oxidation. Active site mutant residues show different fluorescence change profiles. Increasing concentrations of H_2O_2 were added to the T136V and H205A *Cg*-OxyR mutants, and fluorescence changes were monitored over time. The progress curves were fitted to signal exponential equation, and the observed rate constants plotted against the H_2O_2 concentration (n = 3). For the R278Q variant, increasing concentrations of R278Q *Cg*-OxyR were added to 100 μM H_2O_2 and monitored the consumption over time. The progress curves were fitted to simple exponential equations, and the observed rate constants plotted against the R278Q *Cg*-OxyR concentration (n = 3).
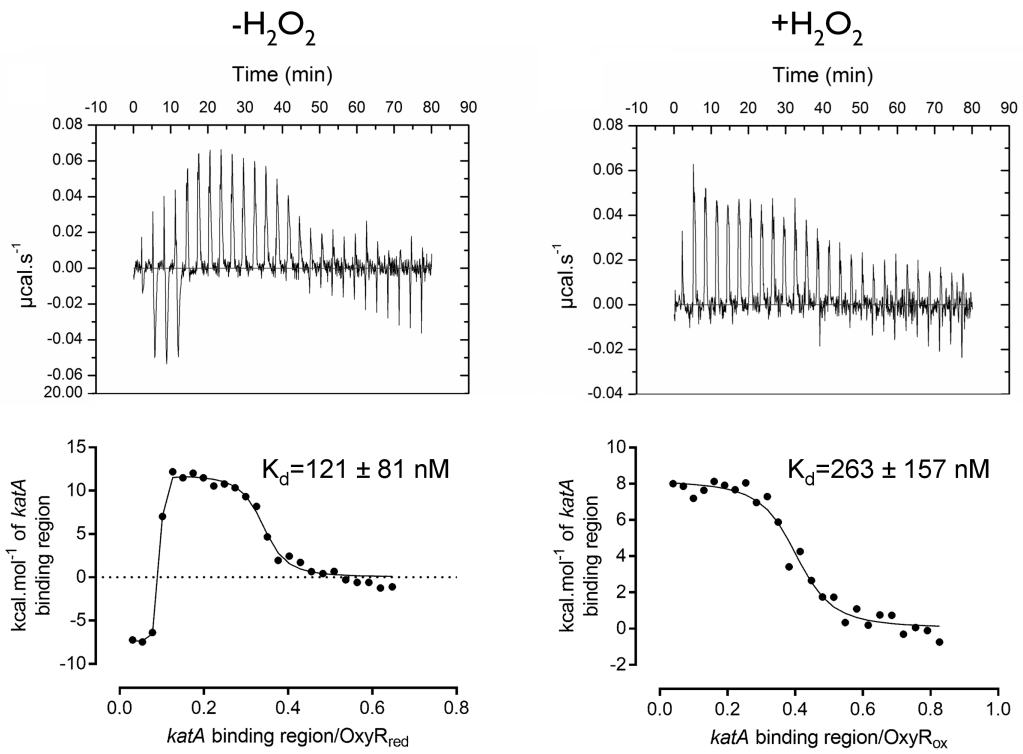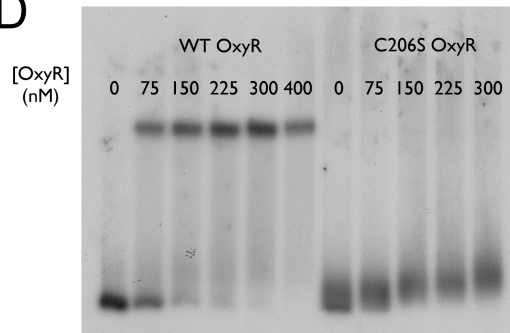
A

[OxyR] (nM)   -H$_2$O$_2$

0 25 50 75 100 120 140 160 180 200 250 300 350 400

[OxyR] (nM)   +H$_2$O$_2$

0 25 50 75 100 120 140 160 180 200 250 300 350 400

B

[RD OxyR] (µM)

0 0.2 0.4 0.6 0.8 1 2 3 4 5 7.5 10 20

C

-H$_2$O$_2$

Time (min)

-10 0 10 20 30 40 50 60 70 80 90

µcal.s^{-1}

K$_d$=121 ± 81 nM

kcal.mol^{-1} of $katA$ binding region

$katA$ binding region/OxyR$_{red}$

+H$_2$O$_2$

Time (min)

-10 0 10 20 30 40 50 60 70 80 90

µcal.s^{-1}

K$_d$=263 ± 157 nM

kcal.mol^{-1} of $katA$ binding region

$katA$ binding region/OxyR$_{ox}$

D

[OxyR] (nM)

WT OxyR   C206S OxyR

0 75 150 225 300 400   0 75 150 225 300

15

Supplementary figure 6: DNA-binding experiments of *Cg*-OxyR to the catalase promoter region. (*A*) EMSA binding profile of *Cg*-OxyR to the catalase operator/promoter region. 10000 counts per minute of a ^{32}P-labelled fragment of the catalase operator/promoter region were mixed with different concentrations of *Cg*-OxyR, in absence or presence of H_2O_2, and then loaded on a 6% acrylamide gel. The upper bands correspond to the protein-DNA complex, while the bottom bands correspond to the free DNA. (*B*) The regulatory domain of *Cg*-OxyR is not involved in DNA binding. 10000 counts per minute of a ^{32}P-labelled fragment of the catalase promoter region were mixed with different concentrations of RD-*Cg*-OxyR. (*C*) Isothermal titration calorimetry experiments support the changes in affinity upon *Cg*-OxyR oxidation. Experiments were performed at 12°C by titrating *katA* binding region, from a stock solution of 112/127 μM, into a solution of 42/37 μM reduced/oxidized *Cg*-OxyR. The isotherms were generated using ORIGIN and the data were analyzed with CHASM (9, 10), employing a nonlinear least squares fitting algorithm. (*D*) C206S *Cg*-OxyR is not suitable for EMSA experiments. Electrophoretic profiles of the ^{32}P-labelled fragment of the catalase promoter region mixed with different concentrations of WT/C206S *Cg*-OxyR.

Hydrazine

-H₂O₂   +H₂O₂   -H₂O₂   +H₂O₂

Citrate
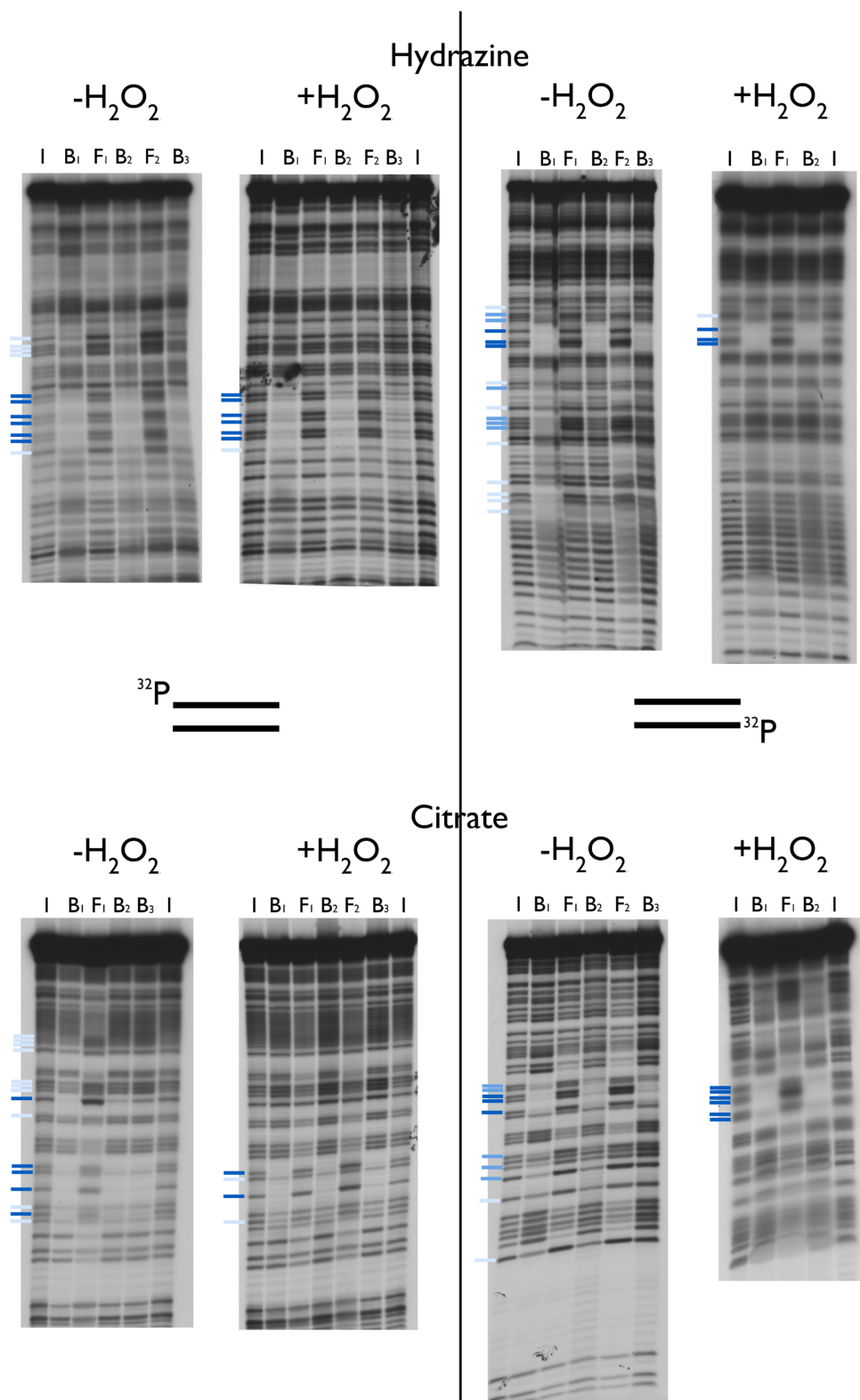
-H₂O₂   +H₂O₂   -H₂O₂   +H₂O₂

```
+H₂O₂
-H₂O₂
CATTCTGATGTAGACTATCAATCAGACTTAATCCATAGGTAACCCTCATAAAAGGAAG
GTAAGACTACATCTGATAGTTAGTCTGAATTAGGTATCCATTGGGAGTATTTTCCTTC
-H₂O₂
+H₂O₂
```

Supplementary Figure 7: Missing contact probing of *Cg*-OxyR binding to the *katA* control region, in presence or absence of H₂O₂. Sparingly modified DNA (citrate for purines, hydrazine for pyrimidines) was incubated with various concentrations of *Cg*-OxyR (1: 150 nM; 2: 225 nM; 3: 300 nM). Protein-DNA complexes were separated from free DNA by native gel electrophoresis. DNA samples that were not incubated with *Cg*-OxyR were included as negative controls [input DNA (I)]. Input DNA, free DNA F, and *Cg*-OxyR-bound DNA B, were eluted from the gel, cleaved at the modified positions and analyzed by denaturing gel electrophoresis. Purine and pyrimidine residues that are directly involved in binding to *Cg*-OxyR are highlighted using blue lines, with the color intensity being proportional to the binding effect. A summary of the results for both strands is presented below, highlighting the -10 region (salmon) and the transcription start point (red).

Supplementary text

Conformational promiscuity in the C_P-C_R disulfide of OxyRs

In the crystal structure of Cg-OxyR$_{SS}$, the C_P-C_R disulfide adopts a –LHStaple configuration. The class of -LHStaple disulfides are notable for their high dihedral strain energy (DSE)(13) and, with an incidence of 1.4% amongst disulfides of crystal structures (14), are relatively rare, even amongst allosteric disulfides. DSE is measured in terms of the torsions angles of the dihedral χ angles of the disulfide, and a high energy DSE is usually indicative of an allosteric disulfide with a functional role. It is striking to note that the C_P-C_R disulfides observed in the oxidized structures of *P. gingivalis* OxyR and *Ec*-OxyR adopt a completely different configuration of -LHSpiral and -LHHook, respectively (Supplementary Fig. 8). Whereas the -LHSpiral disulfide of *Pg*-OxyR is typical for a structural disulfide, with a low DSE and a more distant cysteinyl Cα-Cα separation (5.8 Å), the -LHHook present in *Ec*-OxyR is considered to be a prevalent allosteric disulfide (15). The disulfide of both *Ec*-OxyR and *Cg*-OxyR$_{SS}$ have short cysteinyl Cα-Cα separations of 4.8 Å and 4.7 Å, another indicator of high strain energy for the disulfide. The difference in disulfide configuration between these different analogs of OxyR could relate to a different disulfide reactivity towards intracellular reductants, or may just be a case of promiscuous disulfide isomerization, as it has been observed in some cases that the same allosteric disulfide can exist in differing configurations (14).
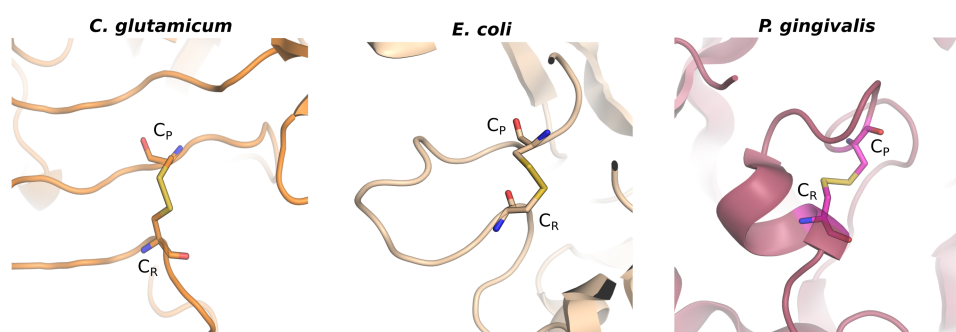
Supplementary Figure 8. Comparison of the different configurations of intramolecular disulfides observed in the structures of *C. glutamicum*, *E. coli* (PDB ID, 1I6A) and *P. gingivalis* OxyR (PDB ID, 3HO7). *C. glutamicum* OxyR (left) adopts a -LHStaple conformation, while in *E. coli* OxyR (middle) a -LHHook disulfide is observed, and *P. gingivalis* OxyR (right) has a –LHSpiral configuration.

Upon disulfide formation, local structural changes exert allosteric influence at the RD homodimer interface of *Cg*-OxyR

The C_P-C_R intramolecular disulfide of *Cg*-OxyR$_{ox}$ is accompanied by unfolding of the RDα3 helix, resulting in the formation of a short β-strand from C206-H208. This unfolding repositions L207 and L214 of the RDα3 into a hydrophobic core lined by L190, L193, L196, L198, L250 and F270. This is accommodated by a 135° χ2 rotation of F172. Further to this, I223 of the flexible loop region succeeding the RDα3 helix is also redirected into

19

the hydrophobic pocket, providing a potential non-covalent contact which may server to draw L200 further into the hydrophobic core, promoting a shift of the loop preceding the now unfolded RDα3. In Cg-OxyR$_{SS}$ the loop region of A228-S234 residing at the RD interface twists into a partial β-strand, disrupting the inter-protomer hydrogen bond between the sidechain hydroxyl of T230 and the backbone amide of I131' of RDβ2' on the opposing protomer (Supplementary Fig. 9B-C). The new conformation of A228-S234 in Cg-OxyR$_{SS}$ forces the RDβ2' strand of the interfacing RD protomer to shift along the interface in order to maintain hydrogen bonding interactions between the backbone peptides. Overall, this requires a combined inter-protomer rotation of 20° in order to reposition the RDβ2' strand (Supplementary Fig. 9A). As a consequence, the RDα1' helix, which typically forms a side-by-side packing against RDα4 in OxyR$_{C206S}$, is instead interlaced between RDα4 and the new conformation of the A228-S234 loop, resulting in an increase in hydrophobic interactions. The RDα4 helix of Cg-OxyR$_{ox}$ appears itself to be 'pulled' towards the newly formed V229-R231, shifting at its N-terminus by approximately 2 Å (Supplementary Fig. 9D), and this rigid body motion is supported by a sidechain flip of -115° (χ1) of W258' of RDα1' to pack between Q240 of RDα4 and R262 of RDα5. This new conformation of the RDα4 helix is then supported by a rotameric switch of both L235 (which resides at the N-terminus of RDα4) and V251 to conserve the non-covalent interaction between these two residues. The combined rigid domain motion of the RDα4 helix and, more significantly, the conformational change of the A228-S234 loop, serve both to disrupt polar interactions at the dimerization interface and introduce a more hydrophobic interaction region. Overall, the structural changes in Cg-OxyR$_{SS}$ lead to an increase in interface surface area of the RD homodimer and concurrent increase in apolar interactions, from ~2375 Å² (12.7% of total surface area) and ~20 apolar interactions in OxyR$_{C206S}$, to 2890 Å² (15.1% of total surface area) and 30 apolar interactions in OxyR$_{SS}$. The replacement of hydrogen bonding inter-protomer interactions with hydrophobic interactions may indicate a less stable OxyR$_{SS}$ RD homodimer compared to the OxyR$_{C206S}$ RD homodimer, and analysis of the respective RD homodimer complexes by the PRODIGY server shows a decrease in calculated ΔG complex affinities of -14.75 and -13 kcal mol^{-1} for the reduced and oxidized homodimeric forms respectively (16). In comparison, the biophysical characteristics of the RD homodimer interface of reduced and oxidized Ec-OxyR appear to be relatively similar, with calculated interface surface areas of 2450 Å² (13.1% of total surface area) and 2260 Å² (12.2% of total surface area) for reduced and oxidized respectively, and comparable predicted complex affinities for the RD homodimers with a ΔG of -10.1 and -10.6 kcal mol^{-1} respectively. As with Cg-OxyR, the C$_P$-C$_R$ disulfide formation in Ec-OxyR also induces formation of a rearranged hydrophobic core in the vicinity of the disulfide, involving L191 (L198 in Cg-OxyR), L239 (L250 in Cg-OxyR) and F209, which is generally non-conserved amongst OxyRs and has a positional equivalent of V229 in Cg-OxyR$_{SS}$ and T230 in Cg-OxyR$_{C206S}$ (17). Relative to Cg-OxyR, the structural changes in the Ec-OxyR RD monomer are more limited to the vicinity of the C$_P$-C$_R$ disulfide region, and as no significant conformational change is evidenced at the RD interface it is less clear which structural determinants drive the significant 30° inter-protomer rotation between the RDs of the Ec-OxyR homodimer, in contrast to the 20° inter-protomer rotation of Cg-OxyR (Supplementary Fig. 10). It is clear that although both isoforms of OxyR undergo the same redox-driven oligomeric change, the biophysical character defining this change is relatively distinct in each of the enzymes.

In the structure of Cg-OxyR$_{C206S}$, each RD subunit forms a minor interface with the RD subunit of the opposing homodimer of $\sim$300-400 Å^2. The interprotomeric rotation of RD subunits observed upon C$_P$-C$_R$ disulfide formation introduces steric overlap at this interface which would serve to disrupt the reduced-form tetramer and allow for rearrangement into the tetrameric configuration observed in the Cg-OxyR$_{SS}$ structure.

*An apostrophe is used to indicate a structural feature of the secondary protomer of the RD homodimer, i.e. RDα1 and RDα1' are α-helices of two separate protomers of the homodimer.
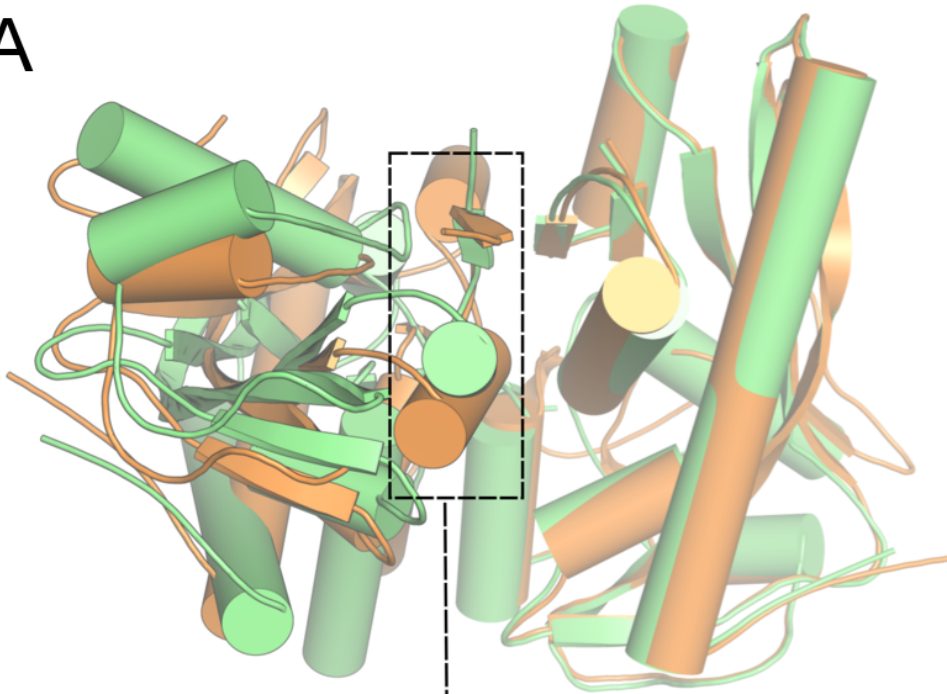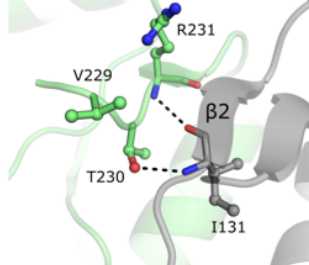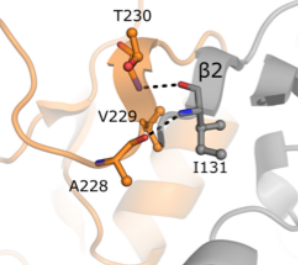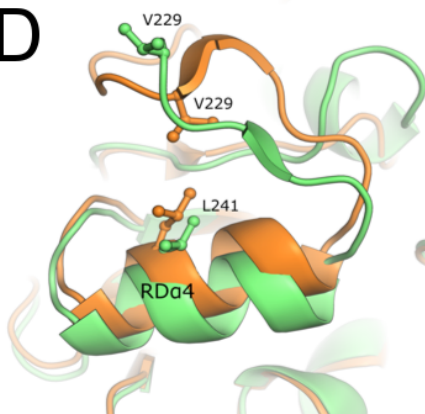
**Supplementary Figure 9**. (*A*) Structural alignment of the RD homodimers of *Cg*-OxyR$_{C206S}$ (green) and *Cg*-OxyR$_{SS}$ (orange). The alignment was performed in PyMOL with the alignment selection limited to a single protomer of the homodimer (right, semi-translucent protomer). (*B*) At the RD dimer interface of *Cg*-OxyR$_{C206S}$, the sidechain hydroxyl of T230 and the backbone amide of R231 form hydrogen bonds with the backbone amide and carbonyl of I131' respectively. Separate protomers are coloured green and grey respectively. (*C*) At the RD dimer interface of *Cg*-OxyR$_{SS}$, I131' instead hydrogen bonds to the backbone amide of T230 and backbone carbonyl of A228. Separate protomers are colored orange and grey respectively. (*D*) The RDα4 helix shifts in conformation in the *C*g-OxyR$_{SS}$ form relative to the *Cg*-OxyRC$_{206S}$ form.
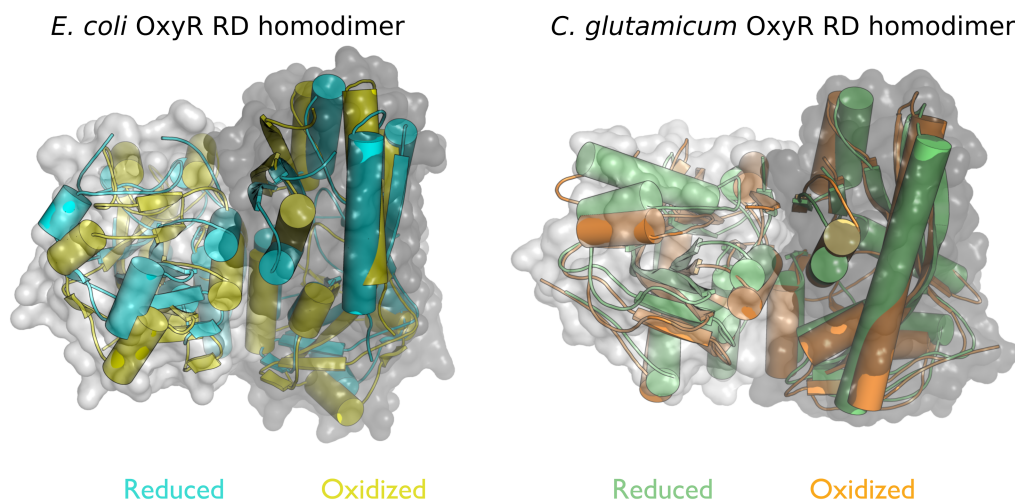
Supplementary Figure 10: Comparative RD homodimer rotation upon oxidation between _E. coli_ OxyR (_Ec_-OxyR) and _C. glutamicum_ OxyR (_Cg_-OxyR). Oxidation of _Ec_-OxyR RD monomer causes a 30° inter-protomer rotation, while the same event in _Cg_-OxyR leads to a 20° inter-protomer rotation only (PDB ID 1I69 and 1I6A for the reduced and oxidized forms of _Ec_-OxyR, respectively (17)).

A conserved region of intermolecular contacts between RD homodimers of the oxidized structures of _E. coli_ and _C. glutamicum_ OxyR

In the presentation of the first published crystal structures of the _E. coli_ OxyR RD, Choi _et al._ emphasized a difference in crystal packing between the reduced and oxidized (C_P-C_R disulfide) RD homodimers (17). They postulated that the pseudotetrameric crystal packing of the oxidized RD reflects its native tetrameric configuration. In superposing the tetrameric _Cg_-OxyR$_{SS}$ with the proposed oxidized _Ec_-OxyR RD pseudotetramer derived from crystal contacts, a striking similarity in the respective assembly of the RD subunits is apparent (Supplementary Fig. 11). In both _Cg_-OxyR$_{SS}$ and the oxidized _Ec_-OxyR pseudotetramer, intermolecular contacts between respective RD homodimers arise at the loop region containing the C_P-C_R disulfide (Supplementary Fig. 11). In the absence of the DBDs, this intermolecular contact between RD subunits would be insufficient to facilitate oligomerization, but may instead be driving specificity for the final tetrameric assembly of the oxidized form. The formation of the C_P-C_R disulfide serves to rigidify a typically flexible region in OxyR. Finally, as described in Supp. Fig. 8, the configuration of the C_P-C_R disulfide loop can vary amongst OxyRs; it can therefore be assumed that a mechanism involving formation of intermolecular contacts at the C_P-C_R loop region may not be universally common to all OxyRs. In _Cg_-OxyR, additional contacts are formed via a 3_{10} helix directly preceding the C_P, however, this region is not well-conserved amongst OxyRs (Supplementary Fig. 11C).
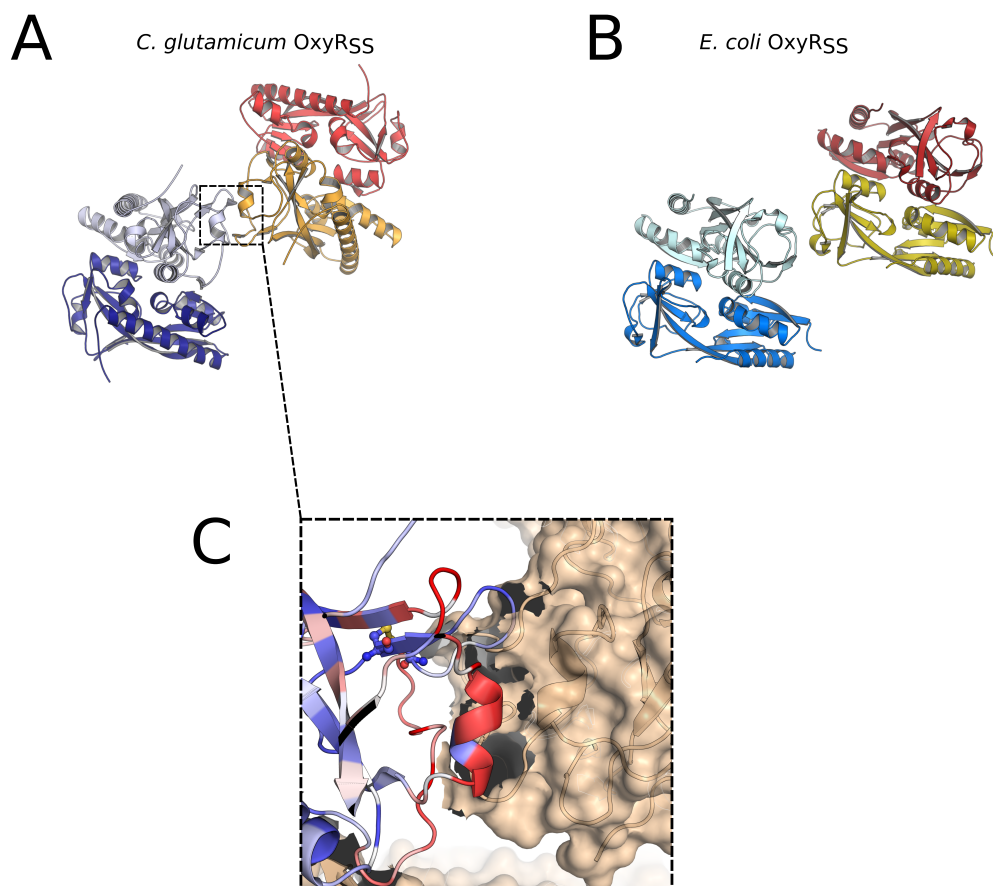
Supplementary Figure 11. A conserved tetrameric arrangement of RD subunits between the oxidized forms of *C. glutamicum* and *E. coli* OxyR. (A) The RD homodimers (with the DBDs consisting of residues 1-100 removed for clarity) of *Cg*-OxyR$_{SS}$ form intermolecular contacts (area within the dotted box) at the region containing the C_P-C_R disulfide. (B). The oxidized crystal structure of *E. coli* OxyR$_{SS}$ also forms intermolecular contacts at the C_P-C_R disulfide region, resulting in intermolecular crystal packing to a pseudotetrameric arrangement of RDs mimicking that of the *Cg*-OxyR$_{SS}$ tetramer. (C) An enhanced view of the intermolecular contact region formed involving the C_P-C_R disulfide loop. The protomer of one RD homodimer (colored gray in panel **A**) is represented as a ribbon structure, colored according to residue conservation as calculated in ConSurf (18-20), as a spectrum from blue (highly conserved) to red (non-conserved). The interfacing protomer of the opposing homodimer is colored pale brown with a surface representation.

### Crystallographic refinement of ligands in the active site pockets of *Cg*-OxyR

In the C_P active site pocket of the crystal structure of *Cg*-OxyR$_{C206S}$, a sulfate molecule was fitted to the available electron density, yet this fitting yielded residual density in the mF_O-DF_C difference map proximal to an oxygen of the sulfate (Supplementary Fig. 12). We are admittedly at a loss as to what occupies this residual density. As this density is ~1.9 Å from the nearest sulfate oxygen, this distance is too short for a metal ion or water molecule, and is instead more likely to be attributable to a covalent bond. A peroxymonosulfate (SO_5H) molecule would fulfil the additional density, but, considering its unstable and highly oxidizing character, its presence is chemically unjustifiable. We additionally solved other isomorphous crystals of *Cg*-OxyR$_{C206S}$, and whilst fitting an

active site sulfate in some gave the same spurious residual density, others showed clearly defined sulfate density in the $2F_O$-F_C map, with no residual density of the F_O-F_C map, this therefore strengthened our confidence in placing an active site sulfate despite residual positive density.

The crystal structure of Cg-OxyR$_{H2O2}$ has a resolution of 2.6 Å, at which resolution some ambiguity may arise in distinguishing covalent bonds (~1.5-2 Å) and strong hydrogen bonds ~2.5 Å. As outlined in the main text of this manuscript, the crystal structure of Cg-OxyR$_{H2O2}$ contains two putative H_2O_2-bound active sites in two respective protomers, termed *Pocket A*, and *Pocket B*. In *Pocket A*, a molecule of H_2O_2 fits well to both a $2mF_O$-DF_C and composite omit map (Supplementary Fig. 13*A* and *B*), whereas fitting of only water molecules gives a poorer fit to the electron density (Supplementary Fig. 13*C*). *Pocket B* suffers more from the ambiguity of distinguishing between covalent and non-covalent interactions at the given resolution, as the density of the active site can be easily fulfilled by either an acetate molecule, or a combination of H_2O_2 and a water molecule. Acetate can derive from the degradation of the crystallization precipitant, polyethylene glycol, however, given the high concentration of H_2O_2 applied in the crystal soak, and considering the only difference between the reduced and H_2O_2-soaked crystallization conditions is the additional presence of H_2O_2, we deemed it significantly more likely that H_2O_2 occupied the available density over acetate. Ethane-1,2-diol can also be modelled with a modest fit to the active site density, though this would result in steric clashes between hydrocarbon hydrogens.

In most crystal structures of OxyR, the side-chain of H205 is in a conformation which directs the Nδ1 into the active site to hydrogen bond with the water/sulfate molecules present. However, in the structure of Cg-OxyR$_{H2O2}$, maximum-likelihood refinement invariably leads to χ2 flip of H205 which directs the Nδ1 away from the active site to instead form a hydrogen bond interaction with D202. This difference in preference of H-bonding partner may derive from a different protonation state of H205 (below pH 6.0, histidine is doubly protonated at its imidazole ring) caused by the addition of H_2O_2 potentially lowering the pH of the crystallization buffer (pH 6.2) by a further 1 pH unit.
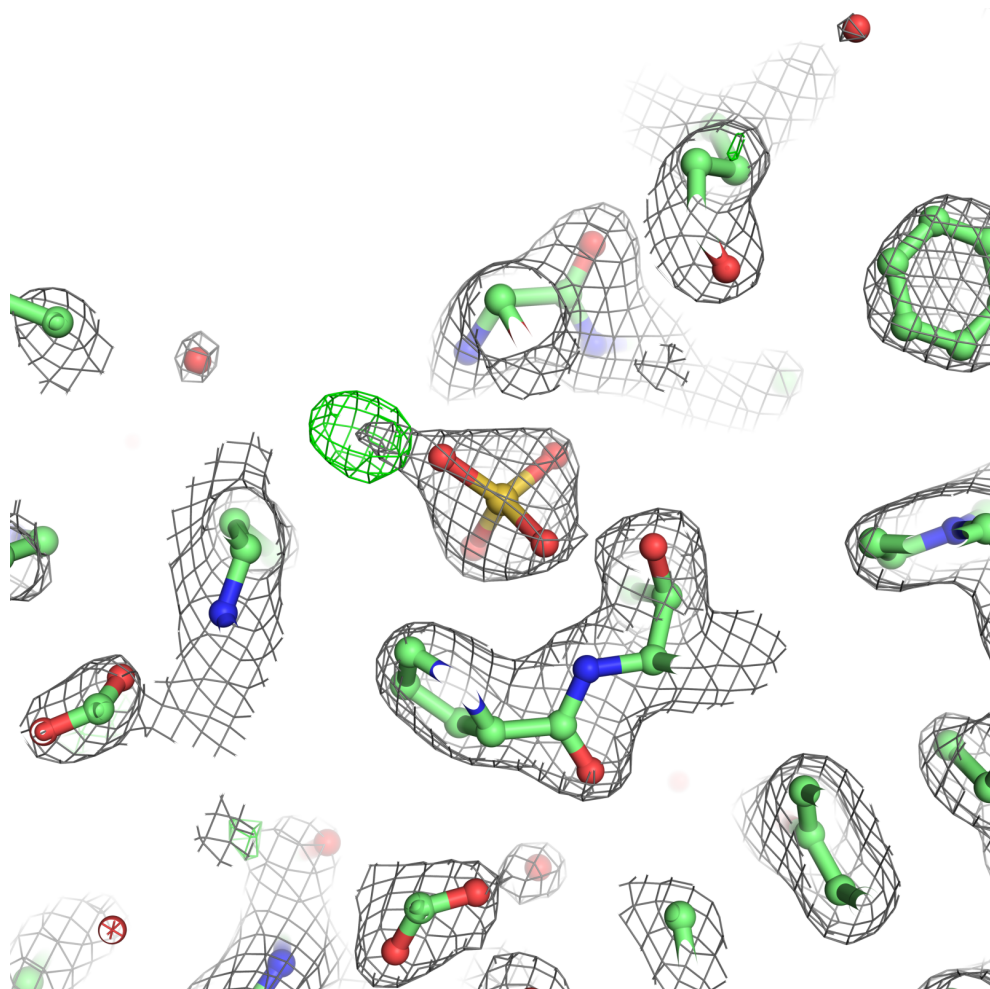
Supplementary Figure 12. Electron density at the active site of *Cg*-OxyR$_{C206S}$. Fitting of a sulfate molecule to the $2mF_O$-DF_C map (grey mesh contoured at 1.6 σ) leaves residual density in the mF_O-DF_C map (green mesh contoured at 3 σ) at a distance from the sulfate oxygen too close for a non-bonding interaction.
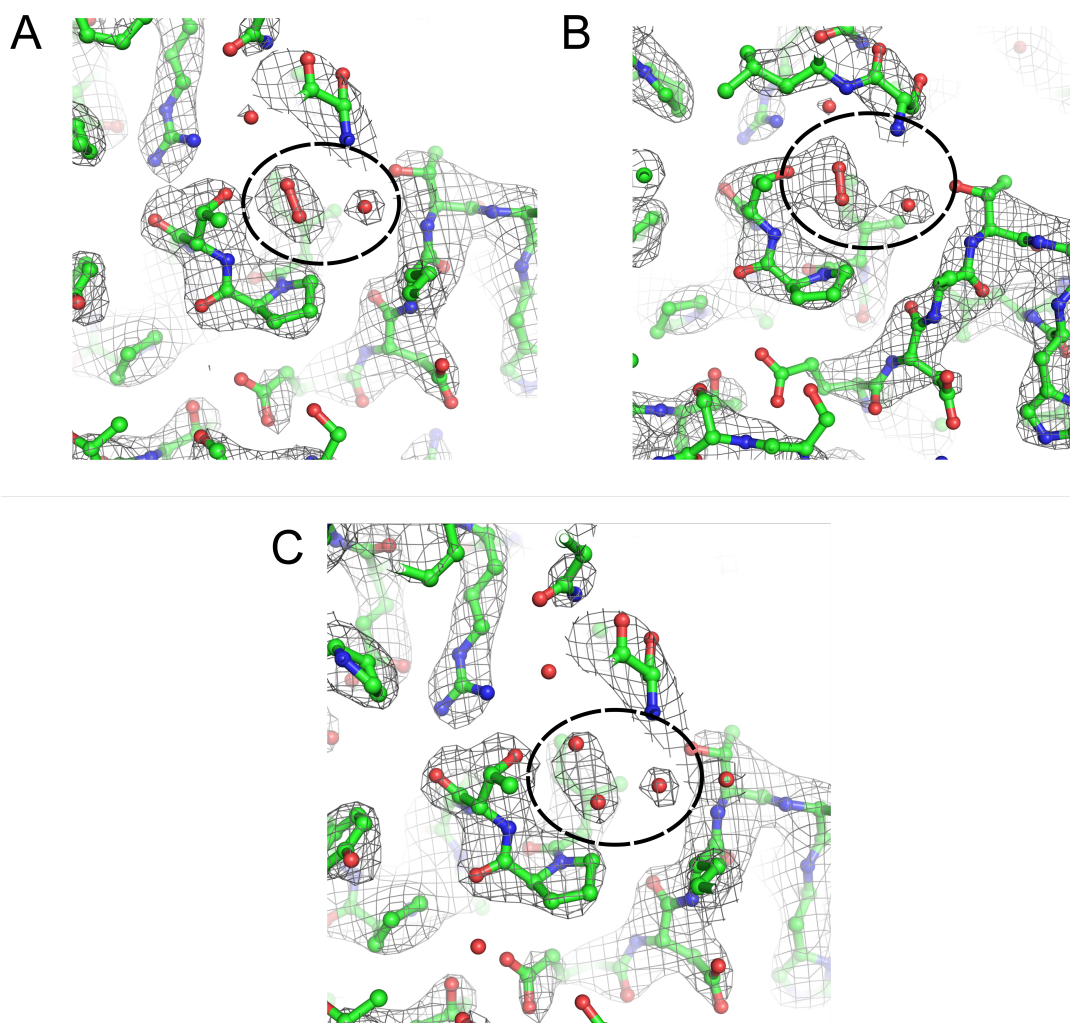
Supplementary Figure 13. Electron density for the molecule of H_2O_2 (red atoms with red bond, hydrogens not displayed) fitted in the active site *Pocket A* of *Cg*-OxyR$_{H2O2}$, with a grey mesh depicting: (*A*) a 2mF$_O$-DF$_C$ map contoured at 1.6 σ, (*B*) a simulated annealing composite omit map contoured at 1.6 σ, and (*C*), a 2mF$_O$-DF$_C$ map contoured at 1.6 σ following maximum-likelihood refinement with two water molecules in place of H_2O_2. A dashed circle is used to draw focus to H_2O_2 and the conserved water molecule forming a hydrogen bond network to T136.

A molecular analysis of the active site pocket of H_2O_2-bound OxyR

For Prdx-mediated catalysis, a water molecule protonates the O$_B$ hydroxide leaving group of H_2O_2 (21), and in the H_2O_2-bound structure of *Cg*-OxyR a water molecule is also present to fulfill this role, itself stabilized by a hydrogen-bonding interaction with T136, whose mutation to valine causes a 100-fold drop in peroxidatic activity relative to wildtype. Differences arise in the molecular geometry of the H_2O_2 binding configurations of *Aeropyrum pernix* Tpx peroxiredoxin (*Ap*-Tpx) and *Cg*-OxyR. In the structure of *Ap*-Tpx, the C$_P$ sulfur forms a quasi-linear complex with H_2O_2, with an Sγ-O$_A$-O$_B$ angle of 172° and a distance of ∼3.5 Å between the C$_P$-Sγ and O$_A$(22). The same angle and distance was observed in the *Ap*-Tpx variant where the C$_P$ was mutated to a serine (22). The linear alignment of H_2O_2 with the C$_P$ sulfur is proposed to represent a reactant state Michaelis

complex conducive for eventual S_N2 nucleophilic substitution, and presents an axis whereupon the Sγ-O_A bond length shortens and the O_A-O_B bond lengthens to form a transition state complex (21). In contrast, the *Cg*-OxyR$_{H2O2}$ presents a non-linear bonding geometry between the C206S hydroxyl and H_2O_2 (for *Pocket A,* a side-chain flip of C206S into the active site is assumed), with an Oγ-O_A-O_B angle of 137°. Assuming that this binding configuration of H_2O_2 in the presence of a C206S mutation is equivalent to the native C_P form, some degree of H_2O_2 rotation should be required to achieve the linear Sγ-O_A-O_B transition state complex favored for an S_N2 reaction. A dynamic change in the binding configuration of H_2O_2 between reactant state and transition state is not an unreasonable supposition as quantum-mechanics/molecular mechanics (QM/MM) simulations of peroxide catalysis by *Mycobacterium tuberculosis* alkyl hydroperoxide reductase E models an Sγ-O_A-O_B angular shift from 94.1° ± 8.3 in reactant state to 161.6° ± 6.2 in transition state with H_2O_2 as substrate (23), and from 105.6° in reactant state to 170.2° in transition state with an alkyl hydroperoxide as substrate (24). As previously mentioned, the protonation state of the active-site H205 of the H_2O_2-bound Cg-OxyR$_{H2O2}$ structure is expected to differ to the protonation state of this residue under neutral buffering conditions; we could therefore speculate that H205 with an unprotonated $N_δ$ may engage as a hydrogen bond acceptor of the O_B-H of H_2O_2, potentially promoting a more linear geometry of Sγ-O_A-O_B.

The binding configuration in *Cg*-OxyR differs to that of the H_2O_2-bound *Pa*-OxyR$_{C199D}$ (25), wherein H_2O_2 bonds to the side-chain hydroxyl of T129 (T136 in *Cg*-OxyR) and one of the carboxyl groups of D199 (originally C199, C206 in *Cg*-OxyR), as well as forming interactions to two water molecules and a backbone amide. This difference in the binding position of H_2O_2 between *Cg*-OxyR$_{C206S}$ and *Pa*-OxyR$_{C199D}$ might be attributed to the steric presence of aspartate at the C_P position in *Pa*-OxyR$_{C199D}$, influencing the active site environment.

Supplementary references

1. Milse J, Petri K, Ruckert C, & Kalinowski J (2014) Transcriptional response of *Corynebacterium glutamicum* ATCC 13032 to hydrogen peroxide stress and characterization of the OxyR regulon. *Journal of biotechnology* 190:40-54.
2. Wang H, Glansdorff N, & Charlier D (1998) The arginine repressor of *Escherichia coli* K-12 makes direct contacts to minor and major groove determinants of the operators. *Journal of molecular biology* 277(4):805-824.
3. Brunelle A & Schleif RF (1987) Missing contact probing of DNA-protein interactions. *Proceedings of the National Academy of Sciences of the United States of America* 84(19):6673-6676.
4. Maxam AM & Gilbert W (1980) Sequencing end-labeled DNA with base-specific chemical cleavages. *Methods in enzymology* 65(1):499-560.
5. Schafer A*, et al.* (1994) Small mobilizable multi-purpose cloning vectors derived from the *Escherichia coli* plasmids pK18 and pK19: selection of defined deletions in the chromosome of *Corynebacterium glutamicum*. *Gene* 145(1):69-73.
6. Letek M*, et al.* (2006) Characterization and use of catabolite-repressed promoters from gluconate genes in *Corynebacterium glutamicum*. *Journal of bacteriology* 188(2):409-423.
7. Villadangos AF*, et al.* (2011) *Corynebacterium glutamicum* survives arsenic stress with arsenate reductases coupled to two distinct redox mechanisms. *Molecular Microbiology* 82(4):998-1014.

8.   Hildebraunt AG & Roots I (1975) Reduced nicotinamide adenine dinucleotide phosphate (NADPH)-dependent formation and breakdown of hydrogen peroxide during mixed function oxidation reactions in liver microsomes. *Archives of biochemistry and biophysics* 171(2):385-397.

9.   Le VH, Yanney M, McGuire M, Sygula A, & Lewis EA (2014) Thermodynamics of Host Guest Interactions between Fullerenes and a Buckycatcher. *J Phys Chem B* 118(41):11956-11964.

10.   Henderson KL, Francis DH, Lewis EA, & Emerson JP (2016) Thermodynamics of substrate binding to the metal site in homoprotocatechuate 2,3-dioxygenase: Using ITC under anaerobic conditions to study enzyme-substrate interactions. *Biochimica et biophysica acta* 1860(5):910-916.

11.   Kumar S, Stecher G, & Tamura K (2016) MEGA7: Molecular Evolutionary Genetics Analysis Version 7.0 for Bigger Datasets. *Mol Biol Evol* 33(7):1870-1874.

12.   Waterhouse AM, Procter JB, Martin DM, Clamp M, & Barton GJ (2009) Jalview Version 2--a multiple sequence alignment editor and analysis workbench. *Bioinformatics* 25(9):1189-1191.

13.   Marques JR, da Fonseca RR, Drury B, & Melo A (2010) Conformational characterization of disulfide bonds: a tool for protein classification. *J Theor Biol* 267(3):388-395.

14.   Schmidt B & Hogg PJ (2007) Search for allosteric disulfide bonds in NMR structures. *BMC Struct Biol* 7:49.

15.   Hogg PJ (2013) Targeting allosteric disulphide bonds in cancer. *Nat Rev Cancer* 13(6):425-431.

16.   Xue LC, Rodrigues JP, Kastritis PL, Bonvin AM, & Vangone A (2016) PRODIGY: a web server for predicting the binding affinity of protein-protein complexes. *Bioinformatics* 32(23):3676-3678.

17.   Choi H, *et al.* (2001) Structural basis of the redox switch in the OxyR transcription factor. *Cell* 105(1):103-113.

18.   Ashkenazy H, *et al.* (2016) ConSurf 2016: an improved methodology to estimate and visualize evolutionary conservation in macromolecules. *Nucleic acids research* 44(W1):W344-350.

19.   Ashkenazy H, Erez E, Martz E, Pupko T, & Ben-Tal N (2010) ConSurf 2010: calculating evolutionary conservation in sequence and structure of proteins and nucleic acids. *Nucleic acids research* 38(Web Server issue):W529-533.

20.   Landau M, *et al.* (2005) ConSurf 2005: the projection of evolutionary conservation scores of residues on protein structures. *Nucleic acids research* 33(Web Server issue):W299-302.

21.   Hall A, Parsonage D, Poole LB, & Karplus PA (2010) Structural evidence that peroxiredoxin catalytic power is based on transition-state stabilization. *Journal of molecular biology* 402(1):194-209.

22.   Nakamura T, *et al.* (2010) Crystal structure of peroxiredoxin from *Aeropyrum pernix* K1 complexed with its substrate, hydrogen peroxide. *J Biochem* 147(1):109-115.

23.   Zeida A, *et al.* (2014) The extraordinary catalytic ability of peroxiredoxins: a combined experimental and QM/MM study on the fast thiol oxidation step. *Chem Commun (Camb)* 50(70):10070-10073.

24.   Zeida A, *et al.* (2015) Molecular Basis of Hydroperoxide Specificity in Peroxiredoxins: The Case of AhpE from *Mycobacterium tuberculosis*. *Biochemistry* 54(49):7237-7247.

25.   Jo I, *et al.* (2015) Structural details of the OxyR peroxide-sensing mechanism. *Proceedings of the National Academy of Sciences of the United States of America* 112(20):6443-6448.